Charting the Dalitz – An exploration of phase-space selection efficiencies within LHCb

Divij Gupta

School of Physics and Astronomy

University of Manchester

MPhys project - Semester 2 report

May 2024

Supervisors: Professor Chris Parkes, Dr David Friday

Abstract

In an era where precision measurements at the LHCb are becoming more prevalent, particularly in the search for CP violation in the charm sector, a robust way to model and compensate for detection asymmetries and detector efficiencies is needed. This report aims to evaluate different methods and tricks that can be used to advise future analyses on how to best mitigate these effects focusing on modelling the efficiency variation across the phase space over determining the absolute efficiency. It also provides a tool to perform this analysis written in Python. At present, this was done for any 3-body decay with the help of Dalitz plots however there is intent to end functionality to higher dimensions with time sensitivity. For the purposes of testing, the decay channel $D^0 \to K_S^0 \pi^+ \pi^-$ using double-tagged samples with DD tracks from 2016 was used. It was found that for binned data, a third-order 2D Chebyshev polynomial best described the efficiency variation and removing the edge bins had no effect on this fit. For symmetric final states, folding the space before performing fits did not affect the results either. For un-binned data, a Kernel Density Estimation (KDE) method was explored. It was found that the choice of bandwidth plays a large role and standard estimation methods such as Scotts and Silverman's are less effective than manual optimisation. However, given the KDE's inaccuracy in modelling variation near edges, further study into this needs to be undertaken. This was attempted through the use of Square Dalitz plots but results were inconclusive and it was undermined whether the optimisation method was too sensitive to these edge effects over modelling the structure of the phase space. This study recommends that future analyses use 2D cubic polynomial fits until this effect can be properly characterised.

Contents

1 Introduction **1**

2 Theory and Detector **2**
2.1 CP violation 2
2.2 LHCb Detector 3
2.3 Dalitz plots 5

3 Methodology and Outline **6**

4 Results and Analysis **7**
4.1 First Look and Efficiency Calcuation 8
4.2 Polynomial Fitting 9
4.3 Stability of Dalitz Space 10
4.3.1 Removing Edge Bins 10
4.3.2 Folding Along the Diagonal 11
4.4 Kernel Density Estimation (KDE) 13
4.4.1 Brief Overview 13
4.4.2 Optimising for the bandwidth 14
4.5 Square Dalitz 16
4.5.1 Re-optimising for the bandwidth 17
4.5.2 Adding reflections 18

5 Conclusion **20**

References **21**

1 Introduction

The Standard Model (SM) of particle physics, shown in Figure 1, is one of the most precisely tested physics theories to date but leaves many questions unanswered. One problem relates to Charge-Parity (CP) transformations, particle-antiparticle transformations, and its violation (CP Violation) which deals with matter-antimatter asymmetries [1]. This report will focus on the investigation of this in quarks.

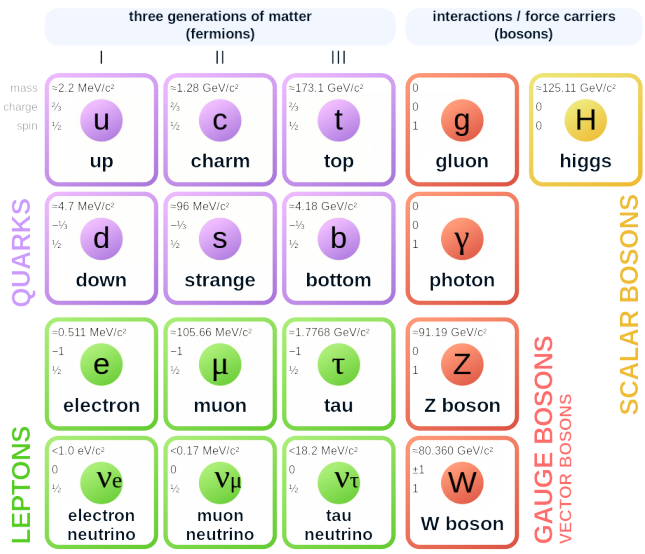

Figure 1: The Standard Model (SM) of elementary particles [2]

According to current models, during the Big Bang equal amounts of matter and antimatter should have been produced and if CP was conserved it should have all annihilated leaving a radiation-dominated universe [1]. However, our presence indicates that matter was favoured ($\sim$1 part in 1 billion [3]) in this process creating a baryon asymmetry indicating that CP must be violated. The mechanism, although not yet fully understood, is called baryogenesis [4] and is part of of one of the 3 Sakharov conditions to lead to the formation of the current observable universe [5].

In the SM, CP violation is included in the Yukawa Lagrangian which looks at Higgs-Fermion couplings [6]. This formalism leads to fermion flavour mixing which in the quark sector is characterised through the Cabibbo-Kobayashi-Maskawa (CKM) matrix [7] [8], V_{CKM}, via a complex weak phase term [9]. This inclusion within the SM, however, is many orders of magnitude lower than what is observed so new Beyond the Standard Model (BSM) physics is needed to introduce additional sources of CP violation [3].

So far most first discoveries of CP violation have relied on 2-body weak decays such as in the kaon system in 1964 [10] (through which CP violation was first discovered) and in the beauty system in 2001 [11]. The results from these experiments agree with the SM and were both awarded the Nobel Prize (in 1980 and 2008 respectively) as they respectively served to motivate and confirm the inclusion of CP violation into the SM. The SM also predicts a small amount of CP violation in the charm sector and statistically significant measurements of it were made in 2019 at LHCb [12] although it is still under current study. The smallness of the predicted value [13] also makes this an interesting playground and avenue for discovering BSM CP violating contributions.

Measurements at the LHCb, and in general modern CP violation measurements (such as at Belle II [14] and BESIII [15]), also incorporate 3-body decays [16] (and even 4-body decays [17] although this report will only focus on the former). In the case of the decay of a flavoured pseudo-scalar meson to 3 flavoured pseudo-scalar daughter mesons, as is often the case, this is done through the use of Dalitz plots which fully characterise the kinematics of the decay space with 2 variables [18]. This allows for the investigation of direct 3-body CP violation but also exploits intermediate resonances to observe a larger multitude of CP-violating 2-body decays directly extracting strong and weak CP violating phases, something which cannot be done in 2-body decays (only a combination can be measured) [3].

Given the current landscape in high precision LHCb searches of CP violation in 3-body charm decays, the smallness of the expected SM CP violation (or BSM contributions) and more statistical data being available than before, minimising all possible sources of error, such as intrinsic systematic uncertainties in the detector, becomes all the more necessary [12]. Characterising the effect of this built-in detector asymmetry in a robust fashion, investigating different techniques to do so and creating a generalised tool for it, all with the help of Dalitz plots, is the goal of this project.

2 Theory and Detector

2.1 CP violation

CP violation refers to the simultaneous breaking of 2 symmetries, charge conjugation (C) which flips the charges of a particle (for example electric charge or colour charge), and parity (P) which flips directions to ensure there is no preferred direction of decay (for example decay rates in x and -x are equal). There also exists time-reversal (T) which reverses the flow of time. From assumptions in quantum field theory, it is assumed that the SM is invariant under CPT implying that any CP asymmetry would lead to a time-reversal asymmetry as well. [19]

As mentioned in Section 1, in the SM CP violation is included as part of the Yukawa Lagrangian in which the strength of the Yukawa coupling terms determine the degree to which quarks couple to the Higgs field. Simplifying the picture greatly and focusing on quarks, in a 3-generation model to allow for physical mass states, the mass mixing terms in the Yukawa matrix need to be removed by diagonalising it which in turn 'moves' the mixing to the quark sector. This allows for mixing between the flavour eigenstates (before diagonalisation) and physical mass eigenstates (after diagonalisation) between different generations of down type quarks through weak interactions [6] [20]. The matrix needed to facilitate this is V_{CKM} named after the people who proposed this formalism and is composed of 3 real rotation angles and one complex CP violating weak phase [7] [8].

There are many ways to investigate this matrix but one prevalent test is testing unitarity as V_{CKM} is expected to be unitary. Unitarity ensures that the number of quarks is conserved in quark transitions (the total probability of transition to all states is unity) a departure from this would indicate BSM physics. Mathematically, depending on the chosen matrix elements, 6 Unitarity Triangles or CKM triangles can be formed (all with the same area) which each being linked to a particular meson (depending on the weak decay involved) [3]. The current global average for this measurement is given in Figure 2 [21] and shows that current measurements are compatible with the assumption of unitarity. More precise measurements of the various angles and side lengths are under further study and constraint [22]. There are also other experiments, outside of unitarity, measuring the magnitudes of the CKM elements directly through specific decay channels [23] which helps parameterise the strength of each coupling.

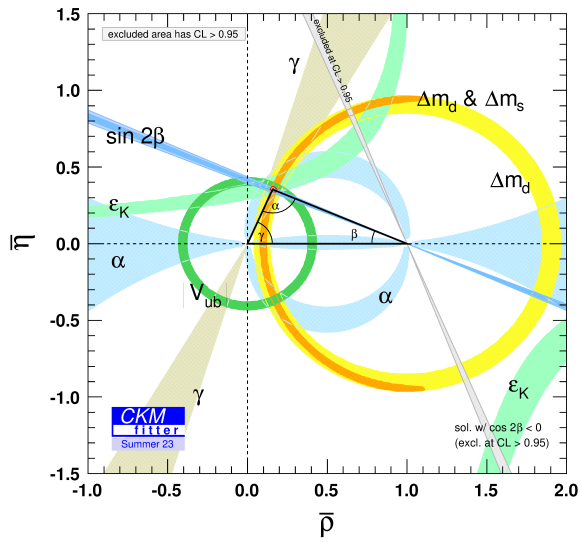

Figure 2: The current global average for the CKM triangle which tests the unitarity of the CKM matrix [21]. ρ and η are variables in the CKM matrix in the Wolfenstein parameterisation [24].

There are in general 3 types of CP violation, weak decays (direct), meson-antimeson mixing (indirect) and interference between both effects (indirect) the later two of which are time-dependent [19]. Currently, in CP violating charm measurements, LHCb focuses on direct measurements via decays which is the motivation and focus of this report [12] [17] [16].

2.2 LHCb Detector

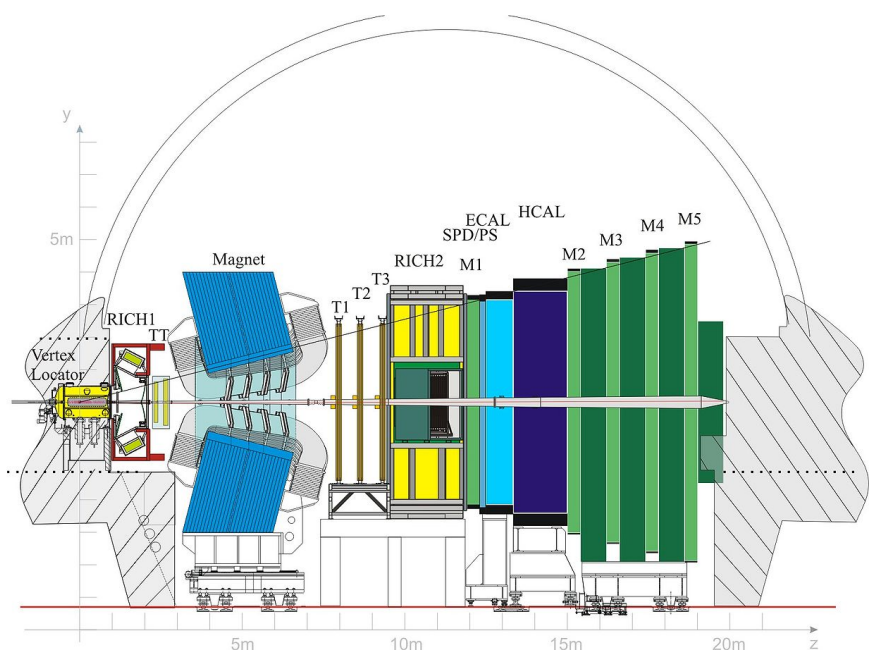

Figure 3: A schematic view of the LHCb detector. The beamline is in the horizontal z-axis and collides in the Vertex Locator to the left of the diagram. The positive (negative) z-axis is known as upstream (downstream). [25]

The Large Hadron Collider Beauty (LHCb) is one of the 4 major experiments at the Large Hadron Collider (LHC) at CERN [26]. Historically it looked at the physics of B-mesons but searches have expanded to precision measurements of CP violation through charm decays (c-quarks) [12], semi-leptonic decays [27], calculations of γ in the CKM matrix [22] (as explained in Section 2.1) and still B-meson physics [28]. The integrated luminosity is $\sim$ 140 fb^{-1} at a centre of mass energy of 13 TeV with pp-collisions [29]. At the moment data for run 3 (2022 - 2025) is being collected and parsed through [30]. A basic schematic layout is shown in Figure 3 [25] and a basic overview is given below.

LHCb is a forward arm spectrometer with a narrow opening angle (pseudo-rapidity range 2 ¡ η ¡ 5 [16]). The pp-interaction point, known as the primary vertex, produces (among other particles) $b\bar{b}$ and $c\bar{c}$ which lead to the production B-meson and D-meson. The decay of these mesons, known as the secondary vertex, both occur in the Vertex Locator (VELO) which is a silicon detector comprised of 26 planes designed to reconstruct the interaction point. Although the LHCb only covers about 2% of the solid angle, it still captures a significant fraction of the $q\bar{q}$ pairs (about 30% of produced $b\bar{b}$ pairs) due to their production mechanism (extremely boosted along the beam-line) [25]. Further downstream the additional Tracker Turicensis (TT) past the VELO also help reconstruct longer tracks. These provide precise information on the charged track position. [12] [31]

Past this, charged particles are bent by a $\sim$ 4 Tm vertical dipole magnet before being sent through three silicon strip detectors with straw tubes filled with gas (Ar_2, CO_2 and O_2), T1, T2 and T3. Charged particles travelling through this gas ionise it and the charge is measured to reconstruct the particle's track. Both of these in tandem can be used to determine the momentum of the charged particle [32]. The direction of the magnetic field is reversed regularly to remove systematic uncertainties from oppositely charged particles being bent into different regions of the detector. [16]

Charged hadrons are distinguished using ring-imaging Cherenkov detectors, RICH2, placed just after T1-3 and RICH1, placed just after the VELO. These exploit the Cherenkov effect [33] where charged particles that travel through gases (CF_4 or C_4F_10) appear to travel locally faster than the speed of light irradiating photons at an angle directly proportional to the particles' velocity. This velocity combined with the momentum information can be used to determine the particle's mass and therefore the type of charged hadron. These play a crucial role in distinguishing different types of mesons. [32] [12]

The final identification state involves a series of calorimeters consisting of a scintillating pad (SPD), pre-shower detectors (PS), an electromagnetic calorimeter (ECAL) and a hydronic calorimeter (HCAL). These contain alternating layers of iron and scintillator, the iron absorbs the particles and the amount of detected scintillation light allows for the determination of the particles' energy. ECAL primarily absorbs photons and electrons (for example from leptoic decays, bremstrallung, radiative decay, etc) and HCAL primarily absorbs hadrons. It is important to note that this is the only part of the detector sensitive to neutral hadrons. The RICH detectors are, in general, more precise than the subsequent calorimiters as hadron showers are messy especially at low energies (HCAL was designed to have only moderate energy resolution [34]). The remaining undetected particles by this point are muons which are detected through M1-5, consisting of alternating layers of gas (Ar_2, CO_2, CF_4) and 'multiwire proportional chambers' designed to detect a signal as the muons travel through the gas, and neutrinos left undetected. [32] [12]

Due to the extreme volume of interactions, about 11MHz of bunch crossings, a trigger is needed to match the disk readout speed of several kHz and store as many events as possible for relevant decay channels being studied. This is first done from hardware information from the calorimeter and muon detectors (1 MHz readout) and then software to reconstruct the full event data and fine-tune event selection

(about 12 kHz readout) [32]. This is the main bottleneck in the study of flavour physics. As a result, detector asymmetries and troubles in resolving nearby particles (expanded upon in Section 2.3), there will always be missing events that pass detection, no part of the detector is 100% efficient, a problem which becomes increasingly prevalent in precision measurements [3].

2.3 Dalitz plots

Dalitz plots (named after Richard Dalitz in 1953 [35]) offer a useful way to visualise the multi-body decay of a pseudo-scalar into pseudo-scalar particles by describing the full phase space and kinematics of the decay in the rest frame of the parent particle [18]. This is generally applied to 3-body decays [36] which is what this report will focus on (in the context of flavoured mesons). This formalism can be adapted to 4-body decays [37] and there is intention for the expansion of this project into that scheme in the future (see Section 5).

The idea in a 3-body decay is that there are 12 degrees of freedom (dof) from the 4-momenta of the 3 final state particles but using 4-momentum conservation (-4 dof), 3 known masses (-3 dof) and 3 Euler angles, representing spacial rotation invariance, (-3 dof) leaves only 2 dof remaining and so decay can be fully characterised using 2 independent quantities. The standard convention is to use two of the three possible 2-body invariant pass pairs as the decay space is a 2D projection of the hyperspace spanned by all the invariant mass pairs (this also helps as intermediate 2-body resonances play a key role in any analysis). This report uses $m_{12}^2 = (p_1^\mu + p_2^\mu)^2$ and $m_{13}^2 = (p_1^\mu + p_3^\mu)^2$. It is also useful to recognise that the third m_{23}^2 axis also exists diagonally 'down' the plots. [38]

The boundaries of this Dalitz plot (known as the kinematic limits) are determined by kinematic conditions and although not derived here (see [18]) are shown in Figure 4. It is also useful to consider, for example, the limits on m_{13}^2 for a given value of m_{12}^2 which determines the shape of the Dalitz. This is done by looking at the m_{12} rest frame and considering parallel and anti-parallel 3-momenta p_1 and p_3 (derivation given in [9]) and are given by:

$$\begin{aligned}(m_{13}^2)_{min} = &\quad (E_1^* + E_3^*)^2 - \left(\sqrt{E_1^{*2} - m_1^2} + \sqrt{E_3^{*2} - m_3^2}\right)^2 \\ (m_{13}^2)_{max} = &\quad (E_1^* + E_3^*)^2 - \left(\sqrt{E_1^{*2} - m_1^2} - \sqrt{E_3^{*2} - m_3^2}\right)^2\end{aligned} \tag{1}$$

where E_1^* and E_3^* are the energies in the m_{12} rest frame given by the standard 2-body decay formulae:

$$\begin{aligned}E_1^* = &\quad \frac{1}{2m_{12}}(m_{12}^2 + m_1^2 - m_2^2) \\ E_3^* = &\quad \frac{1}{2m_{12}}(M^2 + m_{12}^2 - m_3^2)\end{aligned} \tag{2}$$

where M, m_1, m_2 and m_1 are the masses of the parent and 3 daughters respectively. It is straightforward to modify this for the limits on m_{12}^2 given an m_{13}^2 or for different invariant mass pairs.

As eluded to, 3-body decays often occur via a 2-body intermediate state and Dalitz plots are particularly useful in highlighting such resonances. These features appear as regions (bands) of high density in the distribution of events where the number of nodes in each band gives the spin of the intermediate-state particle. Although the details are not explored here, it is useful to have a general overview.

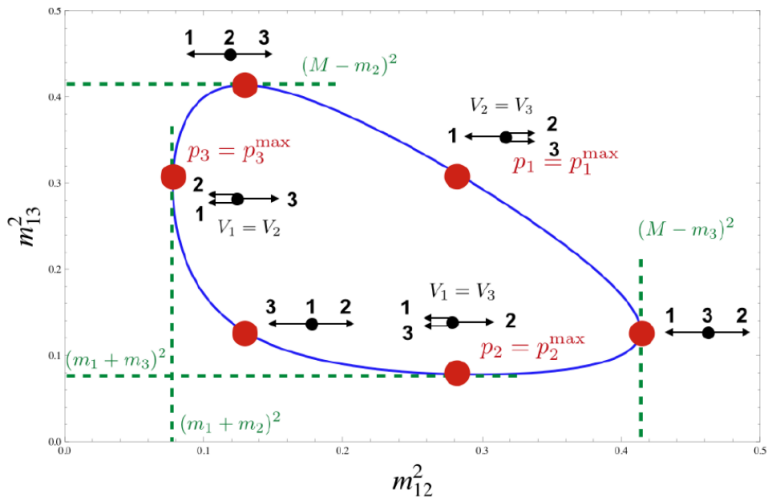

.

Figure 4: An illustrative Dalitz plot for the 3 body decay of a particle in the rest frame of the parent showing the kinematic limits [38]. The third m_{23}^2 axis can also be interpreted to be diagonal 'down' from top right to bottom left. A derivation can be found in [18]

The idea is that there can be several interfering amplitudes from resonances corresponding to different decay modes varying across the space and the local Dalitz plot density is proportional to the total decay amplitude (or the overall matrix element squared in a direct 3-body decay) [18]. CP violation requires 2 interfering amplitudes with different strong and weak phases. The strong phase can be directly measured from the density variation in the Dalitz and the weak phase can be extracted from comparing particle and antiparticle decay plots [3]. CP violation is either directly measured on an event-by-event basis (interference in decay amplitude) or indirectly using the whole plot to calculate helicity angles, the angle of the spin projection to the momentum of the particle [39] , for example (interference in mixing amplitude) [38]. This project will use these plots to characterise detector efficiencies across the phase space.

3 Methodology and Outline

This project aims to characterise intrinsic detector asymmetries which lead to inefficiencies in particle detection which have become increasingly necessary to control as mentioned in Sections 1 and Section 2.2, so far there is no standardised, robust way to do this. The goal is to advise future analyses on best practices and create a generalised tool for efficiency corrections. This was done in Python using Dalitz plots to properly visualise and model how the efficiency changes across the phase space of the decay.

Models and fits are particularly needed when dealing with edge cases, in binned data if two bins have very different efficiencies it's very un-physical to assign a discontinuous jump from one bin to the other especially if the event lies very close to the edge. For this reason, smooth models are preferred, hence the need for fits. The discussion of the detector in Section 2.2 and of the Dalitz space in Figure 4 can be used to get an idea of which areas in the phase space will have high and low efficiencies which is useful in informing which models should be tested.

Assuming the desired parent is produced in the VELO, if it travels too far the decay would happen outside the VELO and not produce any tracks making it very hard to reconstruct although not completely impossible. Looking at the daughter particles, low-momentum charged particles might be bent out of the magnet entirely (and hence the detector) or if they remain within they would produce very messy showers in the HCAL making them hard to reconstruct. High momentum charged particles on the other hand would leave clean trails and less scattering making them easier to detect. In the context of Figure 4, this would respectively create regions of low efficiency near the corners (where one particle is produced at rest in the centre of mass frame) and high efficiency near the edges (where there is maximal momentum of on particle) [40]. Neutral particles have the added difficulty that only the HCAL is sensitive to them making them inherently hard to detect and detection less accurate since the RICH systems (only sensitive to charged particles) have higher resolution than the HCAL, making their understanding particularly interesting. These effects are crudely encapsulated in Figure 5. It should also be noted that the very outer edges of the plot will have very few entries given that they are extreme cases with large errors making them harder to characterise. From this, potentially a degree 3 or higher-order polynomial might be a good starting point to fit this data.

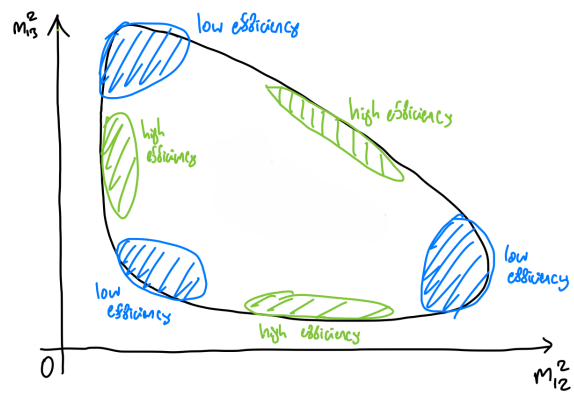

Figure 5: A crude prediction of high and low-efficiency regions on a Dalitz plot given the structure of the LHCb detector based on the discussion in Section 2.2. Blue and green shading represent low and high efficiency regions respectively.

For the purposes of testing, this report will focus on one decay channel, $D^0 \to K^0_S \pi^+ \pi^-$, which was chosen as it is currently under study (relating to CP violation in charm) [41] with available data to use. Importantly, K-short is a neutral short-lived particle that decays into 2 charged pions which helps in that it is easier to reconstruct charged tracks over neutral tracks but given its short lifetime it can be hard to determine where the decay occurred (to make sure it was from a K-short) adding another layer of complexity. Given this, the preceding discussion is particularly relevant and this is a prime example of where proper efficiency characterisation is necessary.

4 Results and Analysis

As only detector asymmetries are being characterised, it is useful to use flat phase space (where the matrix element is constant) to remove any resonance structure from the Dalitz plots. As previously mentioned in Section 3, all the data was generated for the $D^0 \to K^0_S \pi^+ \pi^-$ decay mode. The LHCb data used was Monte Carlo (MC) data from a 'double tagged sample using DD tracks' from 2016 and it represents flat phase space that has been passed through a simulation of the LHCb detector response

making it ideal for explore selection efficiencies. Double tagging refers to how the flavour of the D^0 mesons produced from B-meson decay was determined with 2 muon tags in the detector (the process involves 2 decays hence the 2 tags) and 'DD' stands for 'down-down' which refers the fact that downstream tracks were used (see Figure 3).

The project was done in Python [42] with some help from ROOT [43] (PyROOT) in reading and writing files and generating fake data. Several other libraries were also used like Numpy [44] for data manipulation, MatPlotLib [45] for plotting, SciPy [46] for fitting and later KalePy [47] for KDE testing.

4.1 First Look and Efficiency Calcuation

Before undertaking a deeper analysis, it is important to first establish the basics and discuss how efficiencies are calculated. Preliminary flat phase space data was generated with 300,000 events using ROOT's TGenPhaseSPace Class removing any inbuilt sampling bias to be used as a standard test. This along with the MC data can both be seen in Figure 6. Given the discussion on resonances in Section 2.3, it is also important to consider invariant mass projections in either axis, which are given in Figure 7 for the MC data in Figure 6b. Flat phase space is as expected with no discernible features. The MC data seems to show areas of low efficiency near the corners and high efficiency near the 3 side edges exactly as was hypothesised from Section 3 and in Figure 5 which is promising. As expected there are no discernible structures in the invariant mass projections as there are no resonances in this sample. This also shows that the structure in the space is not from resonances but rather other, detector, effects.

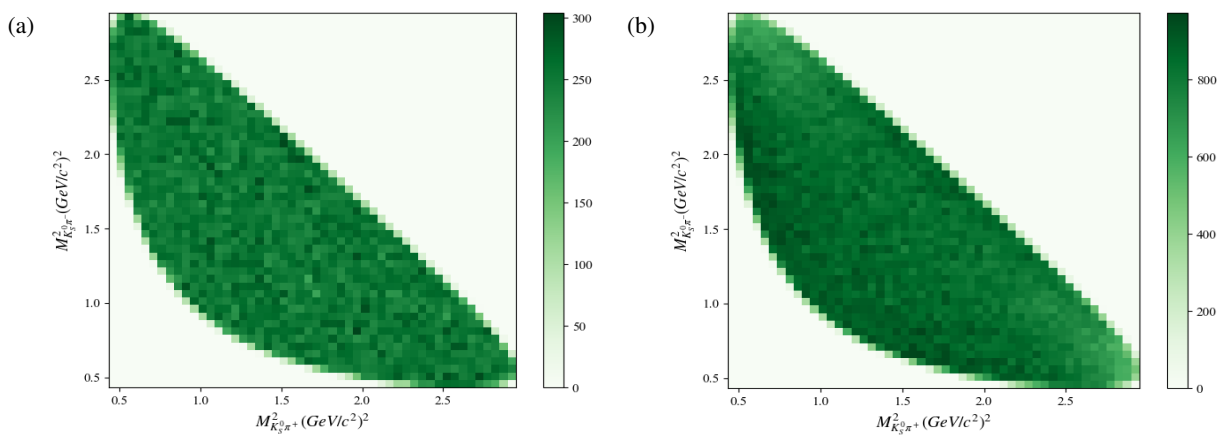

Figure 6: Dalitz plots showing data for the decay channel $D^0 \to K^0_S\pi^+\pi^-$ in the case of (a) flat phase space generated with ROOT's TGenPhaseSpace and (b) LHCb MC data corresponding to flat space that has been passed through a simulation of the detector. Binning is 50x50 uniform.

Comparing the flat space samples to the MC sample an efficiency can be calculated on a bin-by-bin (or point-by-point basis). This is done very simply using:

$$\varepsilon_i = A\frac{N_i^{obs}}{N_i^{true}} \tag{3}$$

where the subscript i refers to the particular bin (or point), ε refers to the efficiency, N_i^{obs} refers to the number of entries after rejection, N_i^{true} refers to the number of entries before rejection (the 'true' number if the detector was 100% efficient) and A is a normalisation that can be used if the samples did not have the same number of entries before rejection. The normalisation was necessary in the MC case as the true

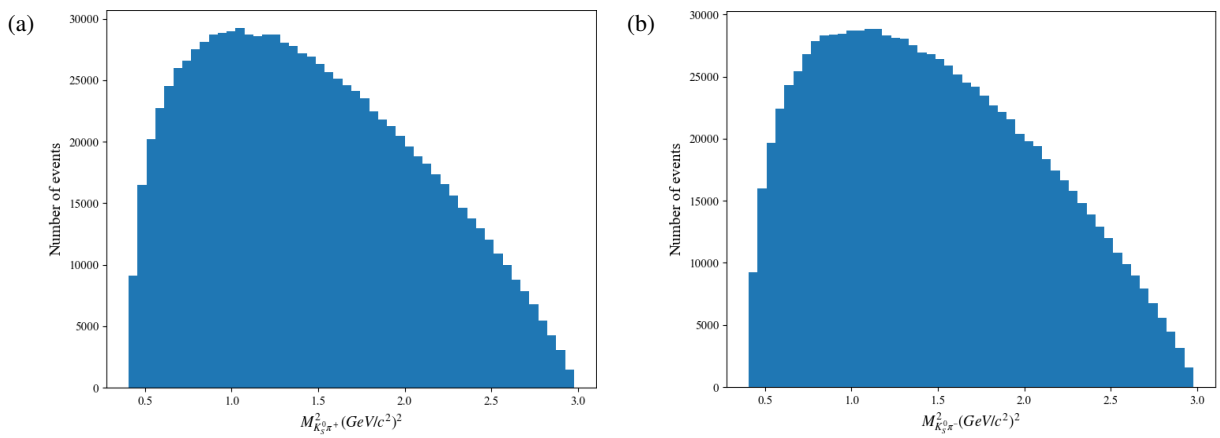

Figure 7: Invariant mass projections for the MC data in Figure 6b in axes (a) $K^0_S\pi^+$ and (b) $K^0_S\pi^-$. Uniform binning with 50 bins.

sample size before detector selection was unknown and was estimated by normalising the pulls plot when testing the fits (explained in Secion 4.2). It is in general not necessary to know the absolute efficiency as long as the variation is properly characterised since, as discussed in Section 2.3, what matters more is the density variation, not the absolute density at a point. A plot of this comparing flat and MC data is given in Figure 8 and aside from hints of very slight low efficiency near the far corners, there are no discernible features present. As mentioned, the efficiency at which the histogram clusters around, ~ 0.4, has no real meaning.

As event selection is a binomial process, binomial errors are assigned to this efficiency as:

$$\sigma_{\varepsilon_i} = \sqrt{\frac{\varepsilon_i(1-\varepsilon_i)}{N_i^{true}}} \tag{4}$$

where all the symbols have their previous meaning. It should be noted however that this is not a straightforward process and this treatment of errors breaks down near efficiencies of 0 or 1 as the formula gives no error when $N_i^{obs} = 0$ or $N_i^{obs} = N_i^{true}$ which is obviously unphysical. There are ways to mitigate this using Bayes Theorem for example [48] [49] but since most relevant analyses are not near either limit (and given that the absolute efficiency can always be tuned enough to avoid this), using Binomial errors is good enough, although it is good to be aware of its limitations.

4.2 Polynomial Fitting

As previously mentioned in Section 3, it is useful to fit smooth models to the efficiency to better characterise the response of the detector. Various 2D polynomials were tested and fit using a least squares fit algorithm assuming Gaussian errors as each bin had enough events (allowed by the central limit theorem). This was done semi-analytically to save computational time (details can be found in [50]). The fit quality was tested using a reduced χ^2 (χ^2 per degree of freedom) and using a plot of the pulls. These are essentially the fit residuals divided by the error and are given by:

$$pulls_i = \frac{\varepsilon_i - \varepsilon_i^{pred}}{\sigma_{\varepsilon_i}} \tag{5}$$

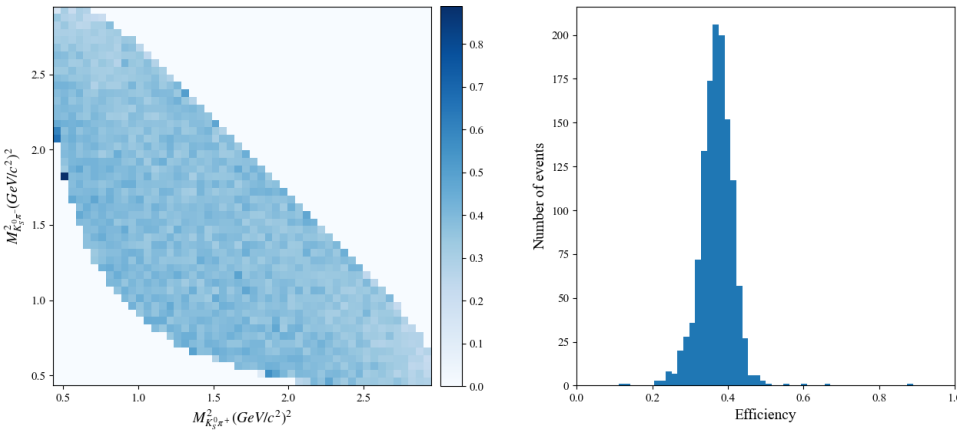

Figure 8: The bin-by-bin efficiency and errors of the MC sample when compared to the flat phase space sample. The normalisation used, explained in Sections 4.1 and 4.2 is 1/9. There is no visible structure.

where i represents the current bin, ε_i is the calculated efficiency, ε_i^{pred} is the predicted efficiency from the fit and σ_{ε_i} is the error on the calculated efficiency [51]. For a good fit, the reduced χ^2 is expected to be ~ 1 and the pulls histogram is expected to be standard normal. Forcing this is how the normalisation factor in the MC sample efficiency given in equation 3 was found (Section 4.1).

The best lowest-order fit to the MC data was achieved with a third-order 2D Chebyshev polynomial. Chebyshev polynomials were used as they eliminate the complexities in fitting that arise from correlated fit parameters (which happens after second-order) by working in a different basis. Plots of this and the pulls are given in Figure 9. The pulls can be seen to be approximately compatible with a standard normal distribution (within error) with no remnant structure visible in the Dalitz space as is expected for a good-quality fit and the χ^2 can be seen to be approximately 1. The slight discrepancy is because there is a heavy dependency on the choice of normalisation and so they should not be fully trusted. Nevertheless, looking at the structure, it can be seen that this is a good model for the overall efficiency across the phase space (there is a longer discussion on this in a previous analysis given in [52]). The fit parameters are not given here as they have no real physical meaning but can be roughly inferred from Figure 10.

4.3 Stability of Dalitz Space

Given the preceding discussion on fits, it's useful to investigate how the space changes given certain constraints and whether this positively or negatively impacts the efficiency fits. This is effectively a test of how stable the Dalitz space is.

4.3.1 Removing Edge Bins

As mentioned in Section 2.3, the very outer edges of the Dalitz plot are often sparsely populated as they correspond to extreme conditions. As a result, those bins carry a large error and may lead to potential biases in the fit so it is interesting to investigate what happens if they were removed. This was done using the kinematic limits given in equation 1 where any bin that lay on the boundary was removed from the fits. Plots of the fits and pulls are not shown here as they do not provide much more information than what is given in Figure 9 but a plot comparing the fit parameters in both cases is shown in Figure 10. From this, it appears that the parameters are compatible with each other indicating the edge bins do not have a

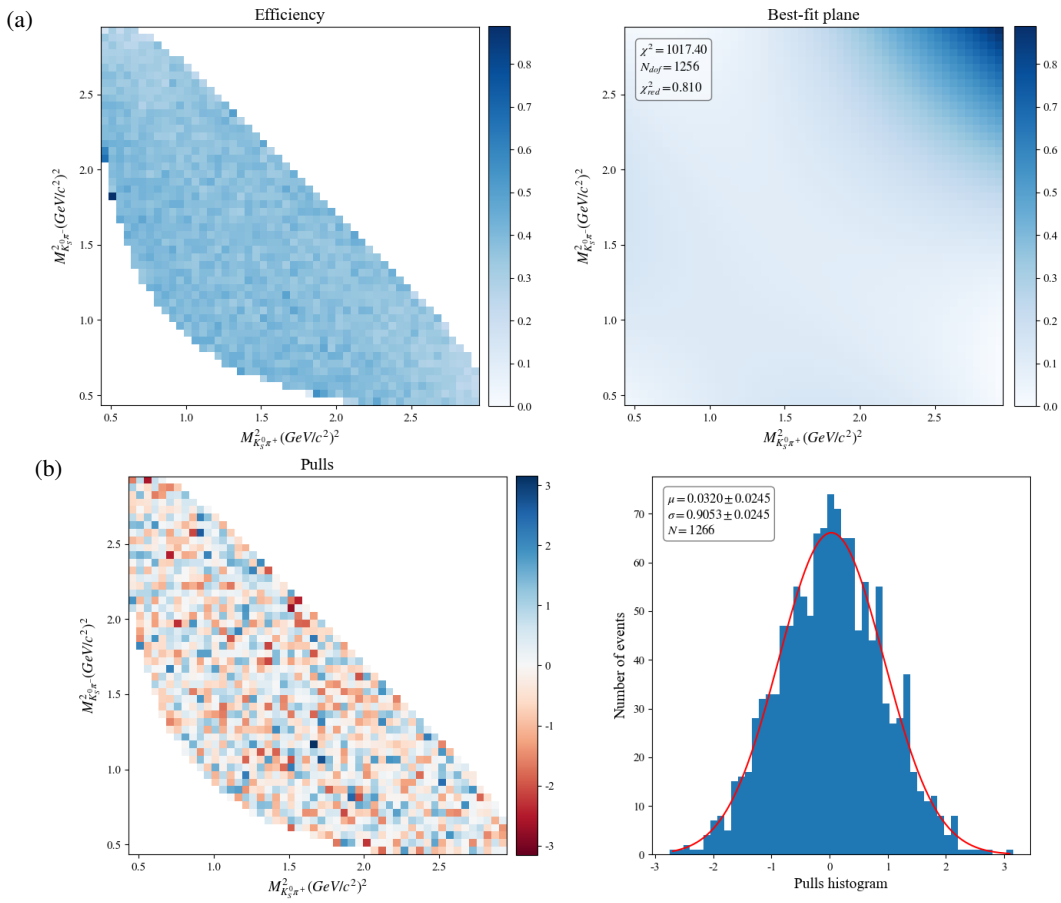

Figure 9: (a) A fit of the efficiency variation in the MC data (left), to a cubic 2D Chebyshev polynomial (right). (b) A plot of the pulls, as defined in equation 5, across the Dalitz space (left) and as a histogram (right). The reduced χ^2 is very close to 1 and the pulls are standard normal indicating this fit is valid.

biasing effect on the fit and need not be removed. This can be important for certain amplitude analyses that contain structure near the edges of the space [53].

4.3.2 Folding Along the Diagonal

Another test can be done by investigating how symmetric the space is. While this is not applicable in all decay channels, for $D^0 \to K^0_S\pi^+\pi^-$ for example it could be useful given the apparent symmetry across the diagonal that can be seen in Figure 6b. This is due to both axes having symmetric final states in π^+ and π^- and therefore serves as a good test to check matter-antimatter detection efficiencies within the detector. This was done by 'folding' one half of the space on top of the other half and looking at the asymmetry between. The equation for doing this is given by:

$$A^i_{asym} = \frac{N^i_1 - \xi N^i_2}{N^i_1 + \xi N^i_2} \tag{6}$$

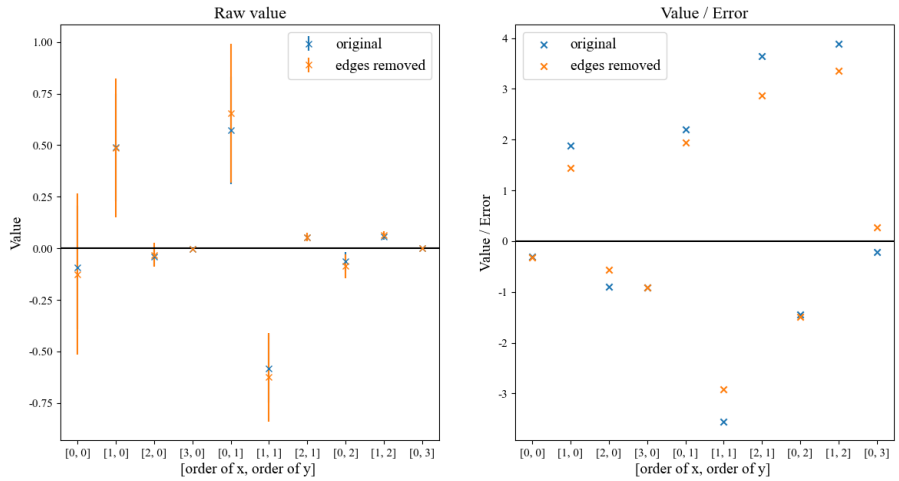

Figure 10: A comparison of the fit parameters obtained from a 2D cubic Chebyshev polynomial fit in the cases where the edge bins were kept and removed. The parameters appear to be compatible with each other.

where are errors are propagated binomial errors given by:

$$\sigma^i_{A^i_{asym}} = \sqrt{\frac{1-(A^i_{asym})^2}{N^i_1 + \xi N^i_2}} \tag{7}$$

where the superscript i refers to the particular bin (or point), A_{asym} refers to the asymmetry, N_1 refers to the number of entries from one sample (one half), N_2 referees to the number of entries from the other sample (the other half) and $\xi = \frac{N^i_1}{N^i_2}$ is the normalisation between them if they have different numbers of entries. The result of this is shown in Figure 11.

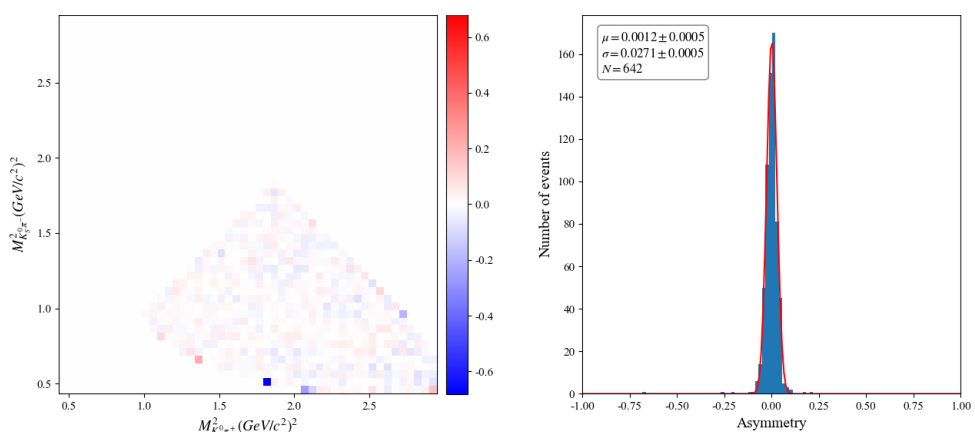

Figure 11: The asymmetry between both halves of the MC Dalitz space split along the diagonal axis. Seems to show no structure indicating that both halves are roughly identical.

In theory, the mass difference between u and d quarks (present in the pions) and the fact that the detector is made of matter not antimatter could introduce a very small detection asymmetry [3] however is not seen in the plot indicating that this effect likely negligible (at least at this resolution). The folded plot was also fit using the same techniques mentioned in Section 4.2 and the difference in fit parameters

is given in Figure 12. As expected from the asymmetry plot, it appears that the parameters are compatible with each other. This shows that folds in cases of symmetric final states are allowed which can be particularly helpful in the case of low statistics as this would effectively double the amount of data available.

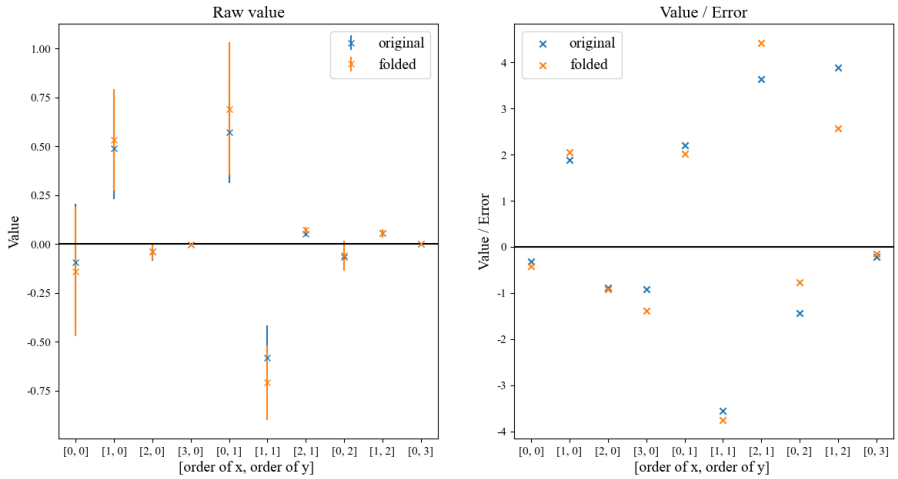

Figure 12: A comparison of the fit parameters obtained from a 2D cubic Chebyshev polynomial fit in original case using the full Dalitz space and in the case where the space was folded along the diagonal. The parameters appear to be compatible with each other.

4.4 Kernel Density Estimation (KDE)

So far the different methods discussed have relied on binning the Dalitz space which itself introduces some uncertainties (the issues with binning were discussed in Section 3 which was the motivation for needing fits). For this reason, it is important to explore unbinned fits which are done here using Kernel Density Estimation (KDE). KDE is a machine-learning algorithm that allows bin and model-independent fitting directly characterising the variation in a given dataset. A normalised KDE can be used to determine the efficiency directly at the exact point in the Daltiz space that it is needed. KDE analysis was done with the help of the aforementioned KalePy package [47].

4.4.1 Brief Overview

Histograms can be thought of as blocks stacked on top of each other with the position of the block dependent on the interval in which the point lies. The issue is changing the bin size/positions heavily changes how the data is presented/modelled. KDEs can be thought of in the same way but each block, known as the kernel, is stacked directly on top of the point instead of being forced into a predefined interval and the overall distribution then is a convolution of these different blocks (adding the heights together at every point). This method is obviously dependent on the choice of kernel although it is common to use Gaussian kernels as they are smooth and somewhat representative of the underlying statistical nature of the events used in such analyses. The other choice of parameter is the width of the kernel known as the bandwidth or smoothing parameter often denoted by h. A large bandwidth gives a very smooth distribution and a small one gives lots of variation. [54]

Figure 13a shows the distribution of points in the Dalitz space for the MC data using this technique where the KDE was trained on the full 2D unbinned dataset before being applied to the same discrete

binning as previously used in Figure 6b. To give the same normalisation as the binned version in Figure 6b this had to be scale corrected using the bin spacing. The bandwidth used is from Silverman's estimation method [55] (one of the standard estimation methods) which gave $h = 0.125$. The other commonly used estimation method, Scotts's [56], gave the same results. The bandwidth can in principle be different in both dimensions however given the symmetry of the space (discussed in Section 4.3.2), the same bandwidth can be used in both cases. Figure 13b shows 1D KDE distribution superimposed on the invariant mass projection histogram of the MC data from Figure 7a using the same bandwidth (KDE retrained with just this projection data and again scale corrected). From both these plots, the KDE can be seen to match the binned data fairly closely giving some credibility to this technique's implementation in this project. The low mass discrepancy in the latter is explored more in Section 4.5.

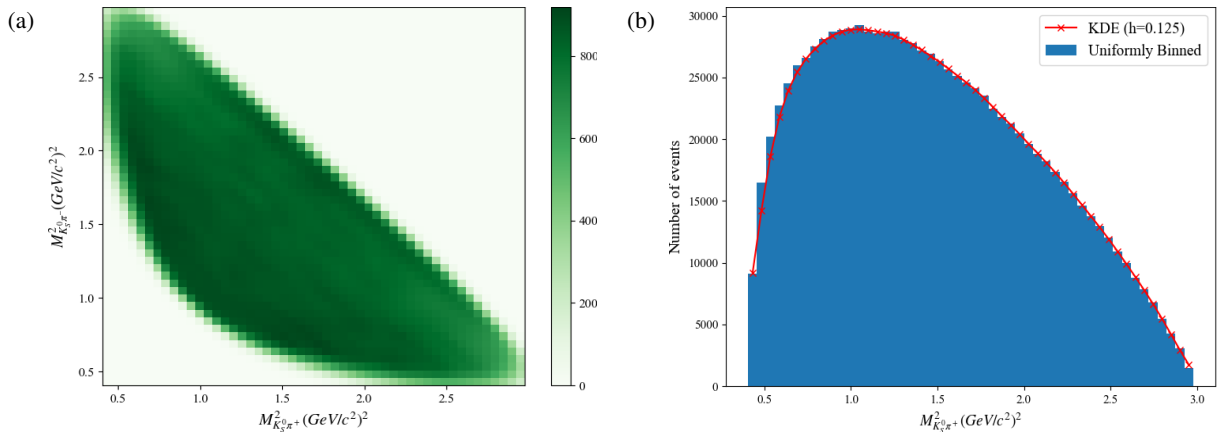

Figure 13: (a) A 2D KDE Dalitz plot for the MC data using a 2D KDE algorithm to recreate Figure 6b. (b) Mass projections of the MC data Dalitz plot with the 1D KDE superimposed to illustrate the difference between the two models. Both KDEs use Gaussian kernels and a bandwidth from Silverman's estimation method [55] of $h = 0.125$ (from the 2D KDE).

4.4.2 Optimising for the bandwidth

Although Figure 13 characterises the variation decently by eye, there seem to be some difference in structure between it and Figure 6b and it is hard to quantify how good the fit is properly. Given this and the lack of estimation methods available to test with, it is useful to try and optimise for the bandwidth manually.

To do this, it becomes necessary to have a 'truth' sample to compare different bandwidth KDE samples with. Given the fits to the MC data discussed in Section 4.2, a sample with cubic structure generated with the same 2D cubic polynomial fit parameters would be ideal as it would mimic the distribution of events from the MC data. This 'cubic rejected' sample was generated using an accept-reject Monte Carlo sampling method. For a given trial bandwidth, the KDE was trained on this cubic rejected sample and then applied to 300,000 points within the Dalitz space from the flat space sample. Using a large number of points and flat space for this is important in making sure no bias is introduced into the test. This was compared with the 'truth' from the fit function evaluated at the same points. It is important to note that in this case the KDE distribution was normalised to both match the truth polynomial and reflect the fact that these are efficiency fits. The comparison was done using a χ^2 test given by the standard

equation:

$$\chi^2 = \sum_i^N \frac{(O_i - E_i)}{E_i} \tag{8}$$

where the sum is over every point in the sampling space, O_i represents the KDE value (observed value) and E_i represents the fit function value (expected value) at a given point.

The results of this are shown in Figure 14. Looking at the zoomed-in right plot, the red best-fit line (a fit to $\chi^2(h) = ae^{-bh} + c + dh$ where a, b, c amd d are fit parameters) indicates that below the minima there is a large change in χ^2 that seems exponential and above the minima there is a much slower linear change in χ^2 with bandwidth. This can be explained by the fact that blow h_{min}, the small bandwidth is sensitive to statistical noise in the data rather than physical features in the phase space and is around detector resolution limits [57]. Above h_{min}, increasing the bandwidth simply smooths out the function bit by bit giving the observed linear variation (as the space is largely linear). As it is computationally intensive to calculate these χ^2 values, the best-fit line can also be used to minimise the χ^2 instead of a direct minimisation algorithm. This gave the optimum bandwidth as $h_{min} = 0.024$. It should be noted that given the nature of the fits and the lack of knowledge on KDE errors, the absolute scale of variation cannot be properly interpreted and is also not necessary for the purposes of this study (see Section 2.3), the variation is most important.

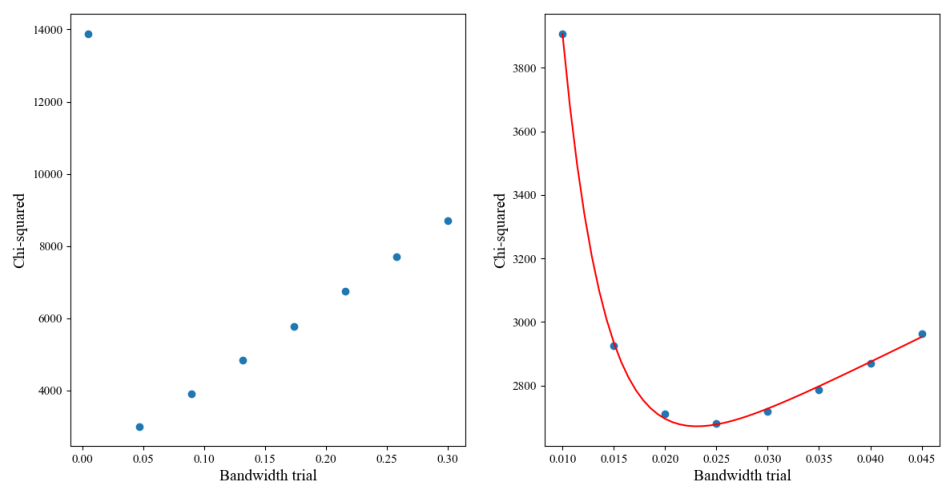

Figure 14: Variation of the χ^2 between the KDE prediction trained on a cubic rejected sample (generated using the 2D cubic polynomial fit to the MC data (see Section 4.2) and the truth (from those fit functions) using 300,000 datapoints. The left plot is an overall scan and the right is zoomed in around the minima. The red best-fit line is to $\chi^2(h) = ae^{-bh} + c + dh$ to roughly model the shape observed and find the minima. The minima is at $h_{min} = 0.024$.

The resulting plot of the Dalitz space for the MC data using this h_{min} is given in Figure 15a which although looking like a good fit isn't particularly enlightening on its own. Figure 15b shows another measure of the fit quality in the form of a histogram representing the asymmetry between the KDE value using h_{min} and the truth, this is also plotted for the value obtained with Silverman's estimation method ($h = 0.125$ given in Figure 13a) to compare the two. The asymmetry is given from Eq. 6 where N_1 and N_2 were taken as the KDE and truth values respectively. From this, h_{min} appears to be a much more sensible bandwidth given the Gaussian shape of the asymmetries which matches what is expected from such a test. Silverman's estimate on the other hand seems to possibly better model certain parts of the

space overall, indicated by the smaller width, but has a very long tail where it always underestimates the true distribution. Given the current limitations in characterising KDE errors, it is hard to properly judge the absolute asymmetry but both KDEs seem to consistently underestimate the truth (as the mean is non-zero). This and the shape of Silverman's estimate's histogram could be a result of edge effects as the edges of the Dalitz are sparsely populated and is explored in Section 4.5.

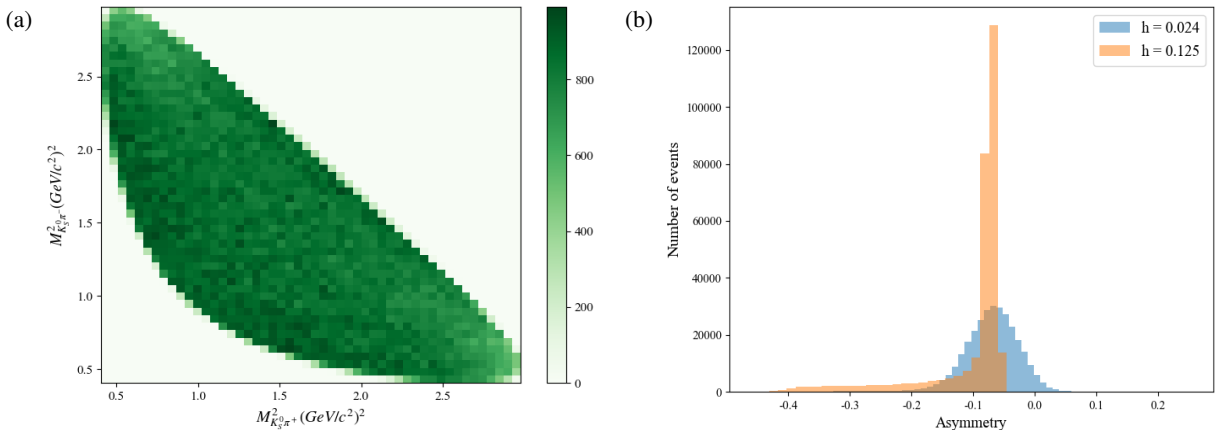

Figure 15: (a) A 2D KDE Dalitz plot for the MC data using the optimised bandwidth (from Figure 14) of $h_{min} = 0.024$. (b) The asymmetry using the cubic rejected data between the KDE predicted values and the truth from the 2D cubic polynomial fits using the optimised bandwidth (blue) and Silverman's estimate (orange). 300,000 evaluation points were used from the flat phase space sample, some points have been removed at the tail end to better show the shape of the distributions

4.5 Square Dalitz

The main issue with KDE, in the context of fits to Dalitz plots, is that predicted distribution must go to zero smoothly at the boundary which is un-physical in practice. The effect of this can almost be seen in Figure 13b by eye with the KDE underestimating the number of entries specifically near the starting edge. This means that the KDE model becomes somewhat unreliable at the edges of the space and the optimisation discussed in Section 4.4 is potentially too sensitive to this rather than the actual structure of the space. It is possible to add reflecting boundary conditions but given the non-uniformity of the space this is hard to do.

The solution is to use Square Dalitz Formalism [18] which is a coordinate transformation defined by:

$$m' = \frac{1}{\pi}\left(2\frac{m_{12} - m_{12}^{min}}{m_{12}^{max} - m_{12}^{min}} - 1\right) \quad \text{and} \quad \theta' = \frac{1}{\pi}\theta_{12} \tag{9}$$

where $m_{12}^{min} = m_1 + m_2$ and $m_{12}^{max} = M - m_3$ are given by the kinematic limits (both can be seen in Figure 4), and θ_{12} is the helicity angle between particles 1 and 3 (the spin of particle 1 projected onto the momentum of particle 3) in the m_{12} rest frame. This is given using:

$$\cos\theta_{12} = -\frac{m_{12}^2 - m_1^2 - m_3^2 - 2E_1^* E_3^*}{2|p_1^*||p_3^*|} \tag{10}$$

where E_1^* and E_3^* are given in Eq. 2 and $|p_1^*|$ and $|p_3^*|$ are the 3-momentum magnitudes which can be

derived from the invariant mass ($|p_i| = \sqrt{E_i^2 - m_i^2}$) all of which are in the m_{12} frame. In the context of this decay mode, M refers to the mass of D^0 and particles 1, 2 and 3 are K_s^0, π^+ and π^- respectively (as has been the case throughout this report). These variables, m' and θ', range between 0 and 1 by design. The resulting plot from this is given in Figure 16 for flat space and MC data using bandwidths of $h = 0.122$ and $h = 0.100$ for both respectively from Silverman's estimation method [55]. Applying reflecting boundary conditions to this becomes much simpler.

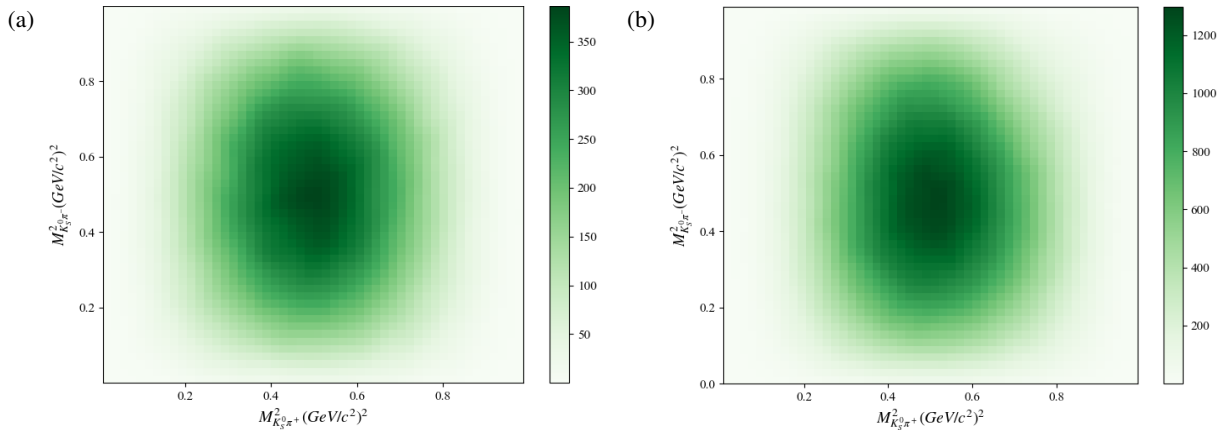

Figure 16: A 2D KDE Square Dalitz plot (as defined from Eq. 9) for (a) flat phase space data and (b) MC data. Bandwidths were from Silverman's estimation method [55] and given as $h = 0.122$ and $h = 0.100$ respectively.

The shape in Figure 16a is typical for flat space and can be explained by the determinant of the jacobian of the transformation which is given by:

$$|\det J| = 4|p_1^*||p_3^*|m_{12}\frac{\partial m_{12}}{\partial m'}\frac{\partial \cos\theta_{12}}{\partial \theta'} \tag{11}$$

where all the variables have their previous meanings. This serves to encapsulate the scaling and volume change of the space as a result of the coordinate transformation. It is important to note that although there is not much difference between the two plots with no visible structure in the MC plot, this is as expected since for this many entries the jacobian structure dominates.

Other than their use here, these coordinate transformations are particularly useful in decays that have resonances very close to the edges of the Dalitz space [53]. This coordinate transformation is designed to enhance these edges to help with such analyses and is also why there is little visible structure in Figure 16b, the structure in the MC data is not close enough to the edge and too faint.

4.5.1 Re-optimising for the bandwidth

Working within this space, the same optimisation was performed as detailed in Section 4.4.2. For this, both the cubic rejected data used to train the KDE and the flat space data that served as evaluation points were transformed into the Square Dalitz space. The added complication in this case was that the 2D cubic 'truth' polynomial is defined in the original space and it is highly non-trivial to transform it into the Square Dalitz space. One way around this is to evaluate the 'truth' in the original space and compare it with the KDE prediction in the square space after removing the jacobian structure from it. This was done by dividing by the jacobian, given in Eq. 11, at any given KDE evaluated point. In principle, the fit

described in Section 4.2 could have been redone in this space but that would make comparisons between different methods much harder. The results from this are shown in Figure 17 and so far this is still without reflections. It should be noted that 100,000 points were sampled for this due to computational constraints.

The shape at higher bandwidths is a little different than in Figure 14 likely as a reflection of this space being non-linear in nature (even if the space is flat due to the jacobian). This also gives much closer bandwidth to Silverman's estimate, with $h_{min} = 0.091$, which is obviously different from what was obtained previously in Section 4.4.2 due to the different scales involved. As the bandwidth is not very different, the Dalitz plot using this would look very similar to Figure 16b. A similar kind of asymmetry plot between the KDE results using h_{min} and Silverman's estimate was done and is given in Figure 19a. In this case, both distributions are virtually identical and seem to suffer from the same tail effects seen in Figure 15b which could again be a result of edge effects although it is unclear as the Square Dalitz plots seems to smoothly go to zero (which is the main thing reflecting boundaries can resolve). The bias towards under-fitting the data seems to have been removed however giving some credibility to this kind of analysis.

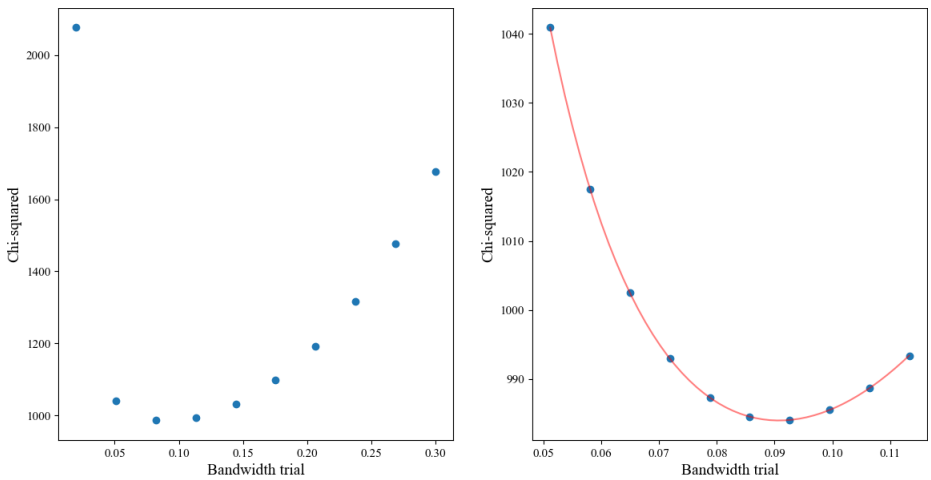

Figure 17: Variation of the χ^2 between the KDE prediction trained on a cubic rejected sample in the Square Dalitz space and the truth evaluated in the original Dalitz space with corrections based on the determinant of the jacobian (Eq. 11) using 100,000 points. The left plot is an overall scan and the right is zoomed in around the minima. The red best-fit line is to $\chi^2(h) = ae^{-bh} + c + dh + eh^2$ to model the shape observed and find the minima. The minima is at $h_{min} = 0.091$.

4.5.2 Adding reflections

Undertaking the same analysis detailed in the previous section (Section 4.5.1) working in the square space but adding reflections gives the plot in Figure 18. It is important to note that Silverman's method is not sensitive to this and so optimises to the same value of $h = 0.100$. As in the previous case, 100,000 points were sampled due to computational constraints. This shows a very similar shape to Figure 17 but with a more pronounced structure parabolic structure around the minima and a more linear variation far away at large bandwidths reminiscent of Figure 14. The minima is given at $h_{min} = 0.062$.

Again, a similar kind of asymmetry plot between the KDE results from this bandwidth and using Silverman's estimate with reflecting boundary conditions is given in Figure 19b. Both plots in Figure 19 seem virtually identical and the same tail effect is still present indicating that it is not a result of edge

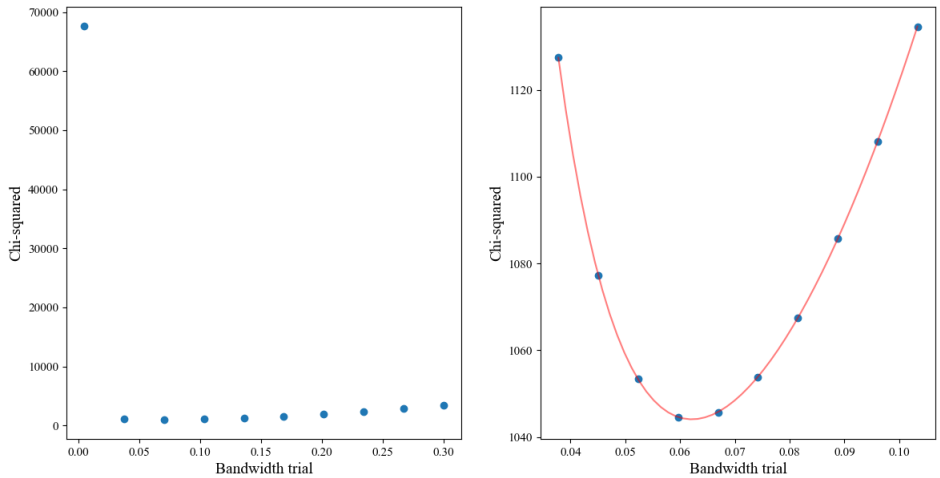

Figure 18: Variation of the χ^2 between the KDE prediction trained on a cubic rejected sample in the Square Dalitz space and the truth evaluated in the original Dalitz space with corrections based on the determinant of the jacobian (Eq. 11) and with reflections added using 100,000 points. The left plot is an overall scan and the right is zoomed in around the minima. The red best-fit line is to $\chi^2(h) = ae^{-bh} + c + dh + eh^2$ to model the shape observed and find the minima. The minima is at $h_{min} = 0.062$.

effects. Given that all the bandwidths give the same result there is likely a systematic error in these fits that has not been properly accounted for or there is some other effect present that is not being modelled. As such the use of Square Dalitz plots to perform this analysis is somewhat inconclusive although the change χ^2 variation plots and observed minima warrant further analysis into why these tail effects are present. Perhaps looking into where in the phase space these tail effects are originating from (both in the normal and Square Dalitz spaces) or looking deeper into the jacobian determinant that has to be corrected for is a good start.

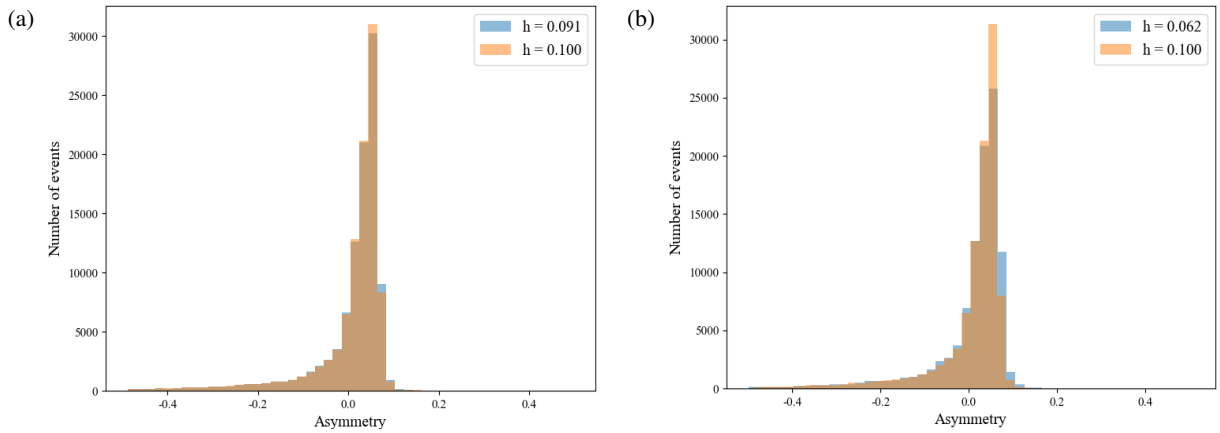

Figure 19: Asymmetry plots using the cubic rejected data between the KDE predicted values in the Square Dalitz space and the truth from the 2D cubic polynomial fits in the original space using the optimised bandwidth (blue) and Silverman's estimate (orange) for the case of (a) 'normal' Square Dalitz space and (b) with reflecting boundary conditions. 100,000 evaluation points were used and some points have been removed at the tail end to better show the shape of the distributions

5 Conclusion

Overall, in the modelling of detector efficiencies, this report shows that in the case of binned data, a cubic 2D polynomial best characterises the variation of the efficiency and removing the bins corresponding to the very edges of the Dalitz space, which are often sparsely populated, has no measurable effect on the resulting fit parameters. For decays to symmetric (CP conjugate) final states, it is perfectly valid to fold the space along the diagonal before performing the fit as it gives the same fit parameters. This in effect showed that the detector being made of matter and not antimatter thus potentially interacting differently with different mass quarks present in the mesons did not affect the resolution in any noticeable way and doesn't need to be corrected for.

In the case of unbinned data, fits using normalised KDE to evaluate the efficiency directly at any given point seem to work well and the bandwidth is better determined manually (as given by Figure 14) to avoid any tail effects from standard estimation methods. Given however that the KDE poorly models the distribution near sharp edges, as in the case in Dalitz plots, it is possible that this bandwidth is too sensitive to the edge effects. To resolve this optimisation in the Square Dalitz space can be used but this investigation was inconclusive as the same tail effects were seen which could not be explained. This requires further analysis.

It is the view of this study that although KDE serves as a powerful tool in characterizing efficiency variation and is able to give the efficiency directly at any point and avoids the effects of binning, it is too sensitive to changes in bandwidth. Until a method to determine the bandwidth can be properly characterised and is known not to be sensitive to sharp edges but rather to model the structure in the phase space, it is better to use a 2D cubic polynomial fit. Once this has been determined, there is intent to extend this discussion into higher dimensions by adding time complexity for example which is necessary for time-dependant CP violating effects present in meson-antimeson mixing .

References

[1] M. Thomson, *Modern particle physics*. New York: Cambridge University Press, 2013.

[2] Cush, "Standard model of elementary particles," 2008. `https://en.wikipedia.org/wiki/File:Standard_Model_of_Elementary_Particles.svg`.

[3] M. Gersabeck, "Frontiers in particle physics ii– part i." University of Manchester, 2024. Lecture Notes.

[4] G. Elor *et al.*, "New Ideas in Baryogenesis: A Snowmass White Paper," in *Snowmass 2021*, March 2022.

[5] A. D. Sakharov, "Violation of CP Invariance, C asymmetry, and baryon asymmetry of the universe," *Pisma Zh. Eksp. Teor. Fiz.*, vol. 5, pp. 32–35, 1967.

[6] M. D. Schwartz, *Quantum Field Theory and the Standard Model*. Cambridge University Press, March 2014.

[7] N. Cabibbo, "Unitary Symmetry and Leptonic Decays," *Phys. Rev. Lett.*, vol. 10, pp. 531–533, 1963.

[8] M. Kobayashi and T. Maskawa, "CP Violation in the Renormalizable Theory of Weak Interaction," *Prog. Theor. Phys.*, vol. 49, pp. 652–657, 1973.

[9] Particle Data Group, R. L. Workman, *et al.*, "Review of Particle Physics," *PTEP*, vol. 2022, p. 083C01, 2022.

[10] J. H. Christenson, J. W. Cronin, V. L. Fitch, and R. Turlay, "Evidence for the 2π Decay of the K_2^0 Meson," *Phys. Rev. Lett.*, vol. 13, pp. 138–140, 1964.

[11] F. Takashi, "The discovery of CP violation in B-meson decays," *Proceedings of the Japan Academy, Series B*, vol. 88, no. 7, pp. 283–298, 2012.

[12] LHCb collaboration, R. Aaij, *et al.*, "Observation of CP Violation in Charm Decays," *Phys. Rev. Lett.*, vol. 122, no. 21, p. 211803, 2019.

[13] A. Lenz and G. Wilkinson, "Mixing and CP Violation in the Charm System," *Ann. Rev. Nucl. Part. Sci.*, vol. 71, pp. 59–85, 2021.

[14] Belle-II collaboration, I. Adachi, *et al.*, "Measurement of *CP* asymmetries in $B^0 \to K_S^0 K_S^0 K_S^0$ decays at Belle II," 3 2024.

[15] BESIII collaboration, M. Ablikim, *et al.*, "Observation of $D \to a_0(980)\pi$ in the decays $D^0 \to \pi^+\pi^-\eta$ and $D^+ \to \pi^+\pi^0\eta$," 4 2024.

[16] LHCb collaboration, R. Aaij, *et al.*, "Search for CP violation in the phase space of $\mathrm{D}^0 \to \pi^-\pi^+\pi^0$ decays with the energy test," *JHEP*, vol. 09, p. 129, 2023. [Erratum: JHEP 04, 040 (2024)].

[17] LHCb collaboration, R. Aaij, *et al.*, "Angular Analysis of $D^0 \to \pi^+\pi^-\mu^+\mu^-$ and $D^0 \to K^+K^-\mu^+\mu^-$ Decays and Search for *CP* Violation," *Phys. Rev. Lett.*, vol. 128, no. 22, p. 221801, 2022.

[18] BaBar collaboration, Belle collaboration, A. J. Bevan, *et al.*, "The Physics of the B Factories," *Eur. Phys. J. C*, vol. 74, p. 3026, 2014.

[19] M. S. Sozzi, *Discrete symmetries and CP violation: From experiment to theory*. 2008.

[20] M. Dasgupta, "Gauge theories." University of Manchester, 2024. Lecture Notes.

[21] CKMfitter Group and W. Qian, "Recent CKMfitter updates on global fits of the CKM matrix," *PoS*, vol. CKM2021, p. 074, 2023.

[22] LHCb collaboration and W. Krupa, "Measurements of the CKM angle gamma at LHCb," *Rev. Mex. Fis. Suppl.*, vol. 3, no. 3, p. 0308057, 2022.

[23] CMS collaboration, A. M. Sirunyan, *et al.*, "Measurement of CKM matrix elements in single top quark t-channel production in proton-proton collisions at $\sqrt{s} = 13$ TeV," *Phys. Lett. B*, vol. 808, p. 135609, 2020.

[24] L. Wolfenstein, "Parametrization of the Kobayashi-Maskawa Matrix," *Phys. Rev. Lett.*, vol. 51, p. 1945, 1983.

[25] LHCb collaboration, J. Alves, A. Augusto, *et al.*, "The LHCb Detector at the LHC," *JINST*, vol. 3, p. S08005, 2008.

[26] CERN, "Experiments," 2024. `https://home.cern/science/experiments`.

[27] F. Ferrari, "Semileptonic B decays at LHCb," *Nuovo Cim. C*, vol. 43, no. 2-3, p. 43, 2020.

[28] LHCb collaboration, R. Aaij, *et al.*, "Measurement of the CKM angle γ and B_s^0-$\bar{B}_s^0$ mixing frequency with $B_s^0 \to D_s^{\mp} h^{\pm}\pi^{\pm}\pi^{\mp}$ decays," *JHEP*, vol. 03, p. 137, 2021.

[29] ATLAS collaboration, "Luminosity determination in pp collisions at $\sqrt{s} = 13$ TeV using the ATLAS detector at the LHC," June 2019.

[30] N. Karastathis *et al.*, "LHC Run 3 Configuration Working Group Report," in *9th LHC Operations Evian Workshop*, (Geneva, Switzerland), pp. 273–284, 2019.

[31] D. Friday, *A time-integrated analysis of $B_d \to \pi^+\pi^-\pi^+\pi^-$ at LHCb and simulations for Low Gain Avalanche Detectors (LGAD)*. PhD thesis, University of Glasgow, 2023.

[32] M. Gersabeck and C. Parkes, "Measuring matter antimatter asymmetries at the large hadron collider." The University of Manchester, September 2023. Third year lab project, Last Accessed: 08/01/2024.

[33] W. R. Leo, *Techniques for Nuclear and Particle Physics Experiments: A How to Approach*. 1987.

[34] R. I. Dzhelyadin, "The LHCb hadron calorimeter," *Nucl. Instrum. Meth. A*, vol. 494, pp. 332–339, 2002.

[35] R. H. Dalitz, "On the analysis of tau-meson data and the nature of the tau-meson," *Phil. Mag. Ser. 7*, vol. 44, pp. 1068–1080, 1953.

[36] LHCb collaboration, R. Aaij, *et al.*, "Amplitude analysis and branching fraction measurement of $B^+ \to D^{*-} D_s^+ \pi^+$ decays," April 2024.

[37] M. Schulz, D. Fischer, T. Ferger, R. Moshammer, and J. Ullrich, "Four-particle dalitz plots to visualize atomic break-up processes," *Journal of Physics B: Atomic, Molecular and Optical Physics*, vol. 40, p. 3091, July 2007.

[38] M. Calvi, "Dalitz plot an introduction." Universita Di Torino, 2016. https://virgilio.mib.infn.it/~calvi/P3/14a.DalitzPlot.pdf, Last Accessed: 07/01/2024.

[39] J. D. Richman, "An Experimenter's Guide to the Helicity Formalism," June 1984.

[40] B. R. Martin and G. Shaw, *Particle physics*. 2008.

[41] T. Gershon and A. Poluektov, "Double Dalitz Plot Analysis of the Decay $B^0 \to D^0 K^+ \pi^-, D \to K_S^0 \pi^+ \pi^-$," *Phys. Rev. D*, vol. 81, p. 014025, 2010.

[42] G. Van Rossum and F. L. Drake, *Python 3 Reference Manual*. Scotts Valley, CA: CreateSpace, 2009.

[43] R. Brun and F. Rademakers, "ROOT - an object oriented data analysis framework," *Nucl. Inst. Meth. in Phys. Res. A*, vol. 389, pp. 81–86, 1997.

[44] C. R. Harris, K. J. Millman, and et. al., "Array programming with NumPy," *Nature*, vol. 585, pp. 357–362, Sept. 2020.

[45] J. D. Hunter, "Matplotlib: A 2d graphics environment," *Computing in Science & Engineering*, vol. 9, no. 3, pp. 90–95, 2007.

[46] P. Virtanen, R. Gommers, and et. al., "SciPy 1.0: Fundamental Algorithms for Scientific Computing in Python," *Nature Methods*, vol. 17, pp. 261–272, 2020.

[47] L. Z. Kelley, "kalepy: a python package for kernel density estimation, sampling and plotting," *Journal of Open Source Software*, vol. 6, no. 57, p. 2784, 2021.

[48] D. Casadei, "Estimating the selection efficiency," *Journal of Instrumentation*, vol. 7, p. P08021–P08021, Aug. 2012.

[49] M. Paterno, "Calculating efficiencies and their uncertainties," December 2004.

[50] T. Nerella, "Phys 240 statistics, data analysis, and machine learning for physicists." University of California, Santa Barbara, 2023. Lecture Notes.

[51] L. Demortier and L. Lyons, "Everything you always wanted to know about pulls." The Rockefeller University, University of Oxford, August 2002. https://hep-physics.rockefeller.edu/luc/technical_reports/cdf5776_pulls.pdf.

[52] D. Gupta, "Charting the dalitz – an exploration of phase-space selection efficiencies within LHCb," Janurary 2024. Master's thesis.

[53] LHCb collaboration, R. Aaij, *et al.*, "Amplitude analysis of $B^0 \to \bar{D}^0 K^+ \pi^-$ decays," *Phys. Rev. D*, vol. 92, no. 1, p. 012012, 2015.

[54] F. Pedregosa, G. Varoquaux, *et al.*, "Scikit-learn: Machine learning in Python," *Journal of Machine Learning Research*, vol. 12, pp. 2825–2830, 2011.

[55] B. Silverman, *Density estimation for statistics and data analysis*. Chapman and Hall, 1986.

[56] D. W. Scott, "On optimal and data-based histograms," *Biometrika*, vol. 66, pp. 605–610, December 1979.

[57] LHCb collaboration, R. Aaij, *et al.*, "LHCb Detector Performance," *Int. J. Mod. Phys. A*, vol. 30, no. 07, p. 1530022, 2015.